


## Article

# First Study of a HEXITEC Detector for Secondary Particle Characterisation during Proton Beam Therapy

Maria L. Perez-Lara <sup>1</sup>, Jia C. Khong <sup>1</sup>, Matthew D. Wilson <sup>2</sup>, Ben D. Cline <sup>2</sup> and Robert M. Moss <sup>1,\*</sup>

<sup>1</sup> Department of Medical Physics and Biomedical Engineering, University College London, London WC1E 6BT, UK; maria.lara.19@ucl.ac.uk (M.L.P.-L.); j.c.khong@ucl.ac.uk (J.C.K.)

<sup>2</sup> Rutherford Appleton Laboratory in the Science and Technology Facilities Council, Chilton OX11 0QX, UK; matt.wilson@stfc.ac.uk (M.D.W.); ben.cline@stfc.ac.uk (B.D.C.)

\* Correspondence: robert.moss@ucl.ac.uk

**Abstract:** Online proton range verification is a rapidly emerging field characterised by its ability to reduce the error margins during proton beam therapy, as it is patient-specific and in vivo. In particular, secondary prompt gamma detection is a promising tool to monitor the dose delivery. The present research evaluates the capability of a HEXITEC detector to identify the prompt gammas produced during proton beam therapy, and assesses its potential for online range verification. To achieve this, the detector is placed at one side of a water phantom, which is irradiated at different proton energies in the University College London Hospital Proton Centre. For further analysis, Monte Carlo simulations are performed using Geant4 and the same geometry as the experiment. The results show that HEXITEC has the potential to be part of a detection system that could identify secondary prompt gammas within the secondary field produced inside the target, allowing for the in-detector discrimination of these particles via cluster size analysis. The comparison between data sets shows that there is a high level of accuracy between the model and the experimental measurements in terms of secondary flux and charge diffusion inside the detector, which poses the model as a fundamental tool for future optimisation studies.

**Keywords:** HEXITEC detector; Geant4; proton beam therapy; prompt gamma detection; proton range monitoring



**Citation:** Perez-Lara, M.L.; Khong, J.C.; Wilson, M.D.; Cline, B.D.; Moss, R.M. First Study of a HEXITEC Detector for Secondary Particle Characterisation during Proton Beam Therapy. *Appl. Sci.* **2023**, *13*, 7735. <https://doi.org/10.3390/app13137735>

Academic Editor: Ioanna Kyriakou

Received: 18 May 2023

Revised: 15 June 2023

Accepted: 28 June 2023

Published: 30 June 2023



**Copyright:** © 2023 by the authors. Licensee MDPI, Basel, Switzerland. This article is an open access article distributed under the terms and conditions of the Creative Commons Attribution (CC BY) license (<https://creativecommons.org/licenses/by/4.0/>).

## 1. Introduction

The radiological use of highly energetic protons has been of interest in the medical physics community since Wilson first discussed the feasibility of proton beams for medical use in 1946 [1]. The main feature that protons offer is the ionisation of tissue with a relatively low and steady linear energy transfer until the proton approaches the end of its range, where its stopping power rises to a maximum. Thus, a proton beam produces a maximum dose at a determined depth (i.e., the proton range), followed by a steep fall-off. This dose-depth curve is known as the Bragg peak, and this interaction between protons and matter is ideal for radiation therapy purposes, where the main goal is to preserve healthy tissue while maximising the treatment dose delivered to the tumour cells. Hence, if the location of the Bragg peak is aligned with that of the tumour, the result is a low dose through the beam trajectory, a maximum dose deposition in the tumour volume, and a dose deposition that is close to zero at depths higher than the proton range, which means a superior sparing of normal tissue and organs that are at risk when compared to conventional radiotherapy with highly energetic X-rays [2].

Proton beam therapy has now been widely used to treat several diseases, including ocular melanomas, base-of-skull cancers (such as chordomas and chondrosarcomas), prostate cancers, head and neck cancers, soft tissue and bone sarcomas, among others [3]. Nonetheless, the main challenges for a high-quality proton therapy treatment are related to the uncertainty in the proton range. During therapy, a radiation dose is given in several

fractions (up to 35), with each fraction having a typical dose delivery of 2 Gy. Typically, the margins of error for proton beam therapy treatments are around 2.5–3% of the proton range, and range from 2 to 3 mm [4]. The uncertainty arises from a wide range of sources, such as variations in the patient's anatomy between fractions (which result in an intrinsic error in the stopping power calculations), the errors during the conversion process from CT images into stopping power maps, and even daily variations regarding the setup and beam settings [5]. Due to this, the development of new methods to perform online proton range monitoring is currently a widely studied area, as they may provide feedback that allows for the treatment to be adapted, with the ultimate goal of reducing the error margins.

Positron emission tomography (PET) systems are considered to be the only clinically available method for 3D range monitoring that is non-invasive, as they measure the positron activity distribution induced by the protons interacting with the irradiated tissue. This method has been studied for particle irradiation offline/after treatment [6], but has longer acquisition times and the risk of not having updated treatment information until treatment has already been delivered. Moreover, there are intrinsic limitations to proton range verification with offline PET/CT systems that introduce errors in the range estimation. The PET signal, which comes from measurable  $\beta^+$  activity, is not identical to the delivered dose. Thus, verification must be obtained by finding a valid comparison between the PET signal and a reference value, which is often calculated with Monte Carlo simulations by simulating activity distributions for different tissues based on the CT information; however, the uncertainties that arise from this comparison have a non-negligible effect on the range estimation, as well as aspects like biological washout (where the radiotracer concentration decreases over time within a specific tissue of interest) and patient motion, suggesting that offline PET range verification is only feasible for a limited number of positions and tumour locations [7]. Due to this, *in vivo* verification studies have also been performed [8–10]. However, the activation process is not immediate: the signal delay varies from seconds to minutes due to the half-lives of the target fragments, which poses several challenges: additional geometrical constraints in the setup to avoid interference with the beam and a consequently more demanding data acquisition system to reduce the large radiation background [11]. Thus, PET systems for this application require optimisation in terms of beam-scanner arrangement, high resolution and efficiency and its combined use with other modalities [12], whilst efforts have also been made to make the acquisition quasi-prompt [13].

The constraints in the PET system as a means of verifying the proton range and monitoring the dose have led to a new focus for state-of-the-art research, based on the exploitation of information coming from secondary radiation that is produced in nuclear interactions between protons and the atomic nuclei inside the body. These particles are emitted along the beam track and they are correlated with the proton dose deposition, which suggests that secondary particle detection can be used to locate the proton range [14]. The production of these particles is due to the fact that, when protons strike a nucleus in the body, the nucleus gets excited and returns to its ground state by emitting particles such as gammas or neutrons, or desintegrates into lighter nuclei [15]. Current imaging systems that detect secondary prompt gammas (PG) focus on finding the production origin, which can be achieved in several ways [16]. Further examples include passive collimation (by a pin-hole, a single slit, multiple slits or knife-edge slit cameras [17]), active collimation (Compton imaging) or using straight PG detection with scintillators (PG ray spectroscopy, PG ray timing, PG peak integration) [18].

Prompt gamma imaging based in scintillators and semiconductor detectors has gained interest in recent decades, given their increased detection efficiency. In particular, semiconductor materials such as CdTe and CZT have a high energetic and spatial resolution for gamma detection, as well as a high scattering probability if the thickness is optimised for this purpose. Furthermore, Compton camera imaging has emerged as a promising method to detect prompt gammas without the need to use physical collimation [19], thus increasing the gamma rates in the detection system. The multi-stage Compton camera concept is based

on a minimum of two detection layers: a scatterer and an absorber. The scatterer should be made of a material with a high Compton scattering cross-section but thin enough to avoid multiple scattering events, whereas the absorber should have a high atomic number and energy resolution such that the scattered gamma deposits the entirety of its remaining energy. The reconstruction process is based on knowledge of the energy deposited in every layer and the location of its deposition, in order to calculate the Compton angle and the initial particle energy via Compton kinematics. By iterating the process with several events, an estimation of the location of the particle source can be achieved.

A number of prompt gamma imaging studies have already been performed for different systems applied to proton beam therapy and show promising results [20–24]. This study aims to exploit the features of the HEXITEC detector [25] in a proton beam therapy monitoring environment, and study its suitability for use in a Compton camera based solely on HEXITEC detector layers. To achieve this, the requirements for suitability include a high spatial and energy resolution for an accurate reconstruction and a high response to gamma particles at the achievable production rates during proton therapy. The gamma response should ideally be higher than the response to other secondary particles for noise reduction. Although originally designed for material science X-ray imaging at energies up to 200 keV, this system has been used for several applications. In particular, its uses in medical physics include spectroscopic X-ray imaging [26,27], SPECT imaging for the brain [28] and targeted alpha therapy [29], but this is the first application of the HEXITEC detector in a proton beam therapy scenario.

## 2. Methods

The main setup of this study consists of a single,  $80 \times 80$ -pixel, Cadmium Zinc Telluride (CZT) HEXITEC detector with a pixel pitch of  $250 \mu\text{m}$  and a crystal thickness of 2 mm, which is placed at one side of a  $50 \times 50 \times 50 \text{ cm}^3$  water phantom, such that the distance between the centres of both objects is 90 cm, as shown in Figure 1. The water phantom is aligned with a proton beam therapy nozzle, and is irradiated for several energies. The nominal proton energies that are analysed in this study are in the range from 75 to 220 MeV, and such protons will naturally produce secondary particles along their track, which we aim to detect.

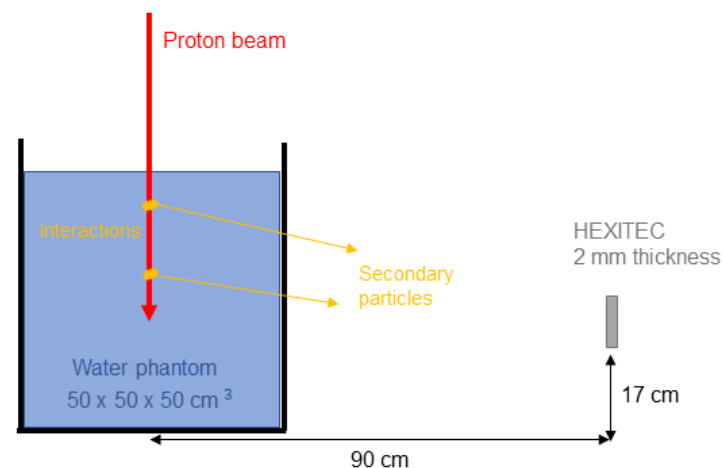


**Figure 1.** Schematic diagram that illustrates the experimental setup. The geometries are kept the same for the experiment at the hospital and the simulations in Geant4.

Although the detector is capable of reading position and energy, there is no information about the incoming particle (i.e., its type or initial kinetic energy). Thus, the present work is subdivided in two forms of data acquisition, which are then compared. These are the experimental and the Monte Carlo model, where the latter outputs additional information that the detector in the experimental setup cannot obtain, such as the particle type. This particular classification method has already been tested with pixellated semiconductor

detectors with the purpose of characterising mixed-radiation fields in terms of type, spectral response and direction of incidence [30].

### 2.1. Experimental Scenario

The first data acquisition was performed at the University College London Hospital (UCLH) Proton Centre, which uses a Varian ProBeam gantry to produce the proton beam. For each proton energy, there is an associated cyclotron current  $I_c$  that is defined by the system. However, the nozzle proton current  $I_{out}$  that will flow to the patient's body is only a fraction of the cyclotron current:

$$I_{out} = \alpha I_c, \quad (1)$$

where  $\alpha$  is an empirical value that will be called the beam factor, which depends on the energy and the gantry angle. These values are nominal conversion factors provided by the proton beamline vendors. Figure 2 shows the behaviour of the proton flux at UCLH for every energy that is relevant to this study, bearing in mind that each proton beam exhibits an intrinsically different primary flux due to the current settings. This is expected to have an effect on the detector flux. The detector is set with a low gain (to be able to record energies up to 700 keV), a bias voltage of  $-1000$  V and a frame rate  $f = 1.6$  kHz. Within the time of a single acquisition frame, the HEXITEC detector can output the location (given by the pixel number in x and y) and energy deposition (given in keV) of every hit. It is additionally important to report that background measurements were taken at the beginning of the experimental data acquisition, where an average of  $0.84 \pm 0.03$  counts per acquisition frame was evidenced. Given that the background signal is not significant, no background correction was performed.

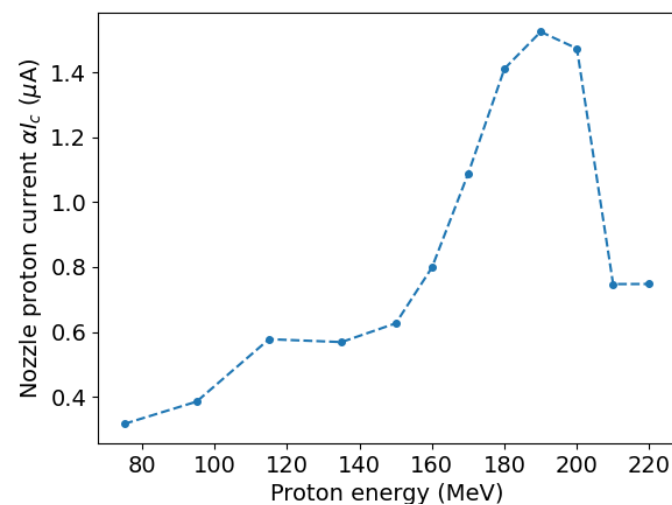


**Figure 2.** Proton current coming out of the beam nozzle for each nominal energy at UCLH.

### 2.2. Simulation Scenario

Monte Carlo calculations were implemented due to the role they play in uncertainty reductions when estimating physical quantities in environments with complex geometries, where a high number of multiple Coulomb scattering events take place. Thus, the second data set was obtained via a dedicated model created in Geant4 (version 10.7) [31] software, which emulates the same geometry used for the data acquisition at UCLH, and is capable of extracting additional physical information of the secondary particles that are produced inside the water target and their potential detection with the detector, which is designed as an array of CZT crystals that match the description of HEXITEC. In addition to the information that can be obtained during the experiment at UCLH, the Geant4 model includes incoming particle information such as event ID, nominal kinetic energy, particle type and parent ID. The latter is key for this study, as it indicates which particle generated the current particle as a result of an interaction or decay. By tracing the parent ID, the history of a

particle can be reconstructed to understand the sequence of interactions or decays that led to its creation. The number of primaries for every simulation set is fixed at  $1 \times 10^9$  for each energy. To account for all relevant physical processes involved in the final output and maximise accuracy, the physics list implemented in the model is QGSP\_BIC\_HP\_EMZ, which includes the most accurate and complete electromagnetic model, the binary cascade model for inelastic nuclear reactions, and the high-precision model to account for radioactive decay. This reference physics list has a high level of accuracy, especially for neutron transport when including the high-precision model [32], and for particular use in proton therapy for secondary particle production, it shows the best agreement with experimental data compared to other lists [33].

### 2.3. Equivalence between Scenarios

Due to the fact that Geant4 gives out the number of primaries, whereas the UCLH experiment gives out one frame every 625  $\mu\text{s}$ , a relationship must be established between both. The number of protons per acquisition frame  $ppf$  is calculated using the primary proton flux:

$$ppf = \frac{I_{out} \cdot t_f}{q_p}, \quad (2)$$

where  $I_{out}$  is defined in Equation (1),  $q_p$  is the proton charge and  $t_f$  is the time per frame, calculated as  $t_f = 1/f$  with  $f$  as the detector frame rate. The number of frames that should be used at UCLH to equalise the number of primaries in Geant4 is defined as

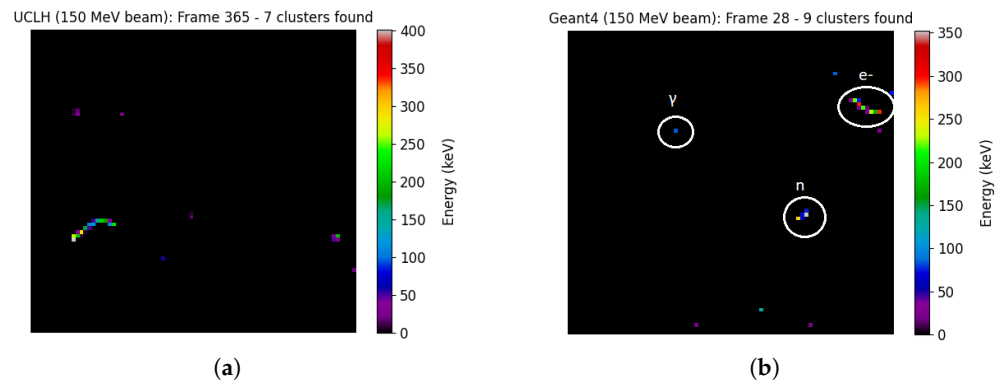
$$N_{frames} = \frac{n}{ppf} = n \cdot f \cdot \frac{q_p}{\alpha I_c}. \quad (3)$$

By using Equation (3) for each energy, the relation between the proton beam energy and the number of frames is found for data analysis. This procedure enables comparable fluxes between UCLH data and simulation. The error in the calculated number of frames results from the systematic fluctuations in the HEXITEC frame rate during acquisition ( $\sigma_f \simeq 11$  Hz), which results in an uncertainty of 0.69% being applied to the number of frames.

## 3. Results

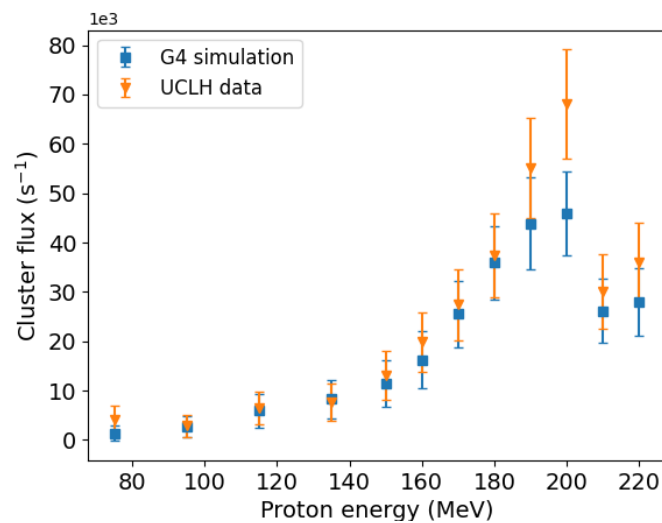
### 3.1. Comparison between Simulation and Experiment

Figure 3a,b are examples of single-frame images that can be obtained from the HEXITEC detector and the simulation detector, respectively, where the simulated image was obtained by framing the data using the number of protons per frame in Equation (2). These images show the detector output in a span of 625  $\mu\text{s}$  when a 150 MeV proton beam is incident on the water phantom, producing secondary particles that will be seen by HEXITEC. Both images depict the interactions between incoming particles and the sensor, where particle tracks and hits are visualised in the form of pixel clusters. Such clustering happens when a particle deposits its energy and the charge produced in the sensor diffuses through more than one pixel. Due to this, the study assumes that a single cluster in a frame corresponds to a single particle entering the detector. This suggests that a characterisation of clusters can be performed such that the cluster size can be related to the particle type, as evidenced from Figure 3b, where the true particle-type information can be retrieved. Whilst electrons produce clusters with a high number of pixels, neutrons and gammas are represented by smaller and more compact clusters.



**Figure 3.** Single frame image produced by the HEXITEC detector during the data acquisition time. Secondary particles produced by a 150 MeV proton beam are detected and their energy deposition can be seen in a 2D histogram. By evaluating the particle type in the simulations, electrons are represented by long track-like clusters, whereas gammas and neutrons have smaller cluster sizes. (a) Image acquired at UCLH. (b) Image simulated in Geant4.

Data clustering was performed for both scenarios using the Python DBSCAN function from the Scikit-Learn [34] package, where the frame number and the position of the events were chosen as the clustering parameters to get the overall total flux in the detector. Figure 4 shows the cluster flux in the detector during the whole experiment for both scenarios. Note that both curves exhibit a similar behaviour that matches the shape of the curve in Figure 2, as expected.



**Figure 4.** Comparison plot showing the total number of clusters per second found in both scenarios.

Although the comparison suggests that the model accurately simulates the experimental setup in terms of secondary particle flux, some dissimilarities are evidenced, especially for the beam energies with the highest beam currents. A definite cause for this is the increase in the background flux in the hospital, which is not taken into account in these measurements, suggesting that a profound characterisation of the background noise should be part of future studies. Additional sources of dissimilarity between UCLH data and the simulation can be attributed to the fact that the latter does not account for the effect of backscattering inside the detector ASIC or housing, as the detector is simplified as a pixellated CZT crystal, and it also does not model the charge transport within the sensitive volume, as this is beyond the scope of the Geant4 software.

### 3.2. Secondary Particle Characterisation

From the simulations performed in Geant4, a further characterisation of the secondary particles created within the primary beam axis was performed. It was estimated that, within the proton energy range used in this study, the number of secondary gammas (i.e., with a parent ID greater than or equal to 1 and for any value of kinetic energy) produced per primary proton ranges between 0.07 and 0.39, depending on the proton energy. In terms of the contribution of gammas and neutrons to the total amount of secondary particles produced inside the phantom, 43–63% of all secondaries correspond to gammas and 19–27% to neutrons, bearing in mind that the gamma percentage decreases with increasing beam energy, whereas the neutron percentage increases with increasing beam energy. To obtain information about the particles entering the detector area, a dummy volume was created right in front of the sensitive detector to read out the incoming flux, as well as the particle type, kinetic energy and parent ID. The secondary gamma yield in the detector area is much lower, ranging from  $6.6 \times 10^{-7}$  to  $5.98 \times 10^{-7}$  per primary proton. Moreover, the particle-type information evidences a dominance of gamma particles, where more than 80% of all interacting particles in the detector are gammas, in spite of the fact that, in reality, they comprise a lower percentage of all secondaries. This suggests that the detection system favours gamma detection over other particles, and the noise that may come from neutrons, electrons, positrons and isotopes is discarded by the system. In particular, neutrons, which are the most common secondary particles produced during treatment after gammas, have a low probability of interaction with the sensor material, but other particles, such as electrons and other isotopes, need a deeper analysis to be filtered out.

A cluster size analysis was conducted to test the previously stated hypothesis where the noise reduction coming from other particles can be achieved by discriminating events in virtue of their cluster size. Figure 5 displays the result of such a discrimination process. Each bin value is obtained by calculating the fraction of particles with a determined cluster size over all secondaries. The values are calculated for each proton beam energy and then averaged. The reported data in the figure are the average, with the error bars representing the standard deviation.

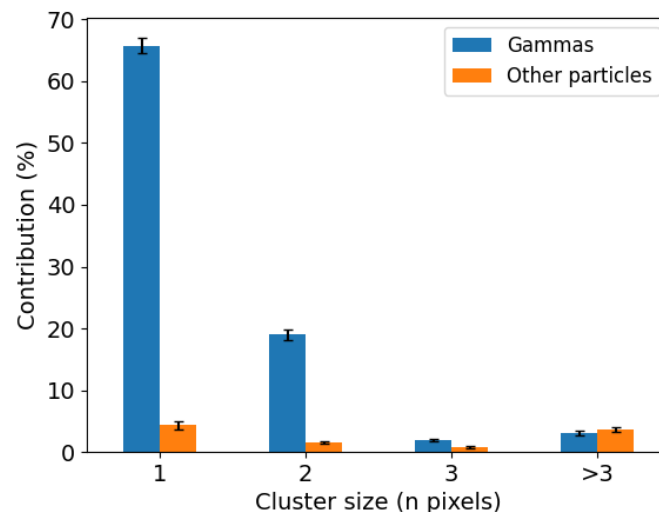


**Figure 5.** Cluster size histogram showing the differences in contribution between gammas and other particles. The sum of all bins (gammas and other particles together) equals 100%. The values are averaged over all proton energies and the error bars are obtained from the standard deviation.

It can be seen that, of all secondary particles detected by HEXITEC, around 65% of them were one-pixel-cluster gammas, which is expected: for the pixel pitch of this detector, there is not a high level of charge-sharing for gamma particles. This implies that a simple threshold in the cluster size removes a significant proportion of background events that are not of interest. Furthermore, the graph suggests that other particles such as neutrons

and electrons can be filtered from the data set via cluster size alone, given that their mean values are above three pixels. This is because, on the one hand, neutrons interact with the detector via multiple scattering, neutron capture (as Cd has a considerable cross-section for this physical process), among others, which causes new particles to be produced and deposit energy at further distances from the original hit. However, they can potentially be identified as they typically scatter before being captured. The subsequent relaxation emits a gamma that usually escapes the detector volume. On the other hand, charged particles such as electrons, scattered protons and positrons may interact with the sensor with a high probability of Coulomb interaction with the sensor material, depositing their energy in several steps and creating a track-like cluster.

For a more in-depth look at the cluster sizes of the most common particles detected in the system, Figure 6 makes use of Geant4 simulation data to create a comparison graph between gammas, electrons and neutrons in terms of their mean cluster size for each beam energy. Particles such as positrons and scattered protons are not included in this graph since they are not present for all energies. The figure reinforces the theory that, by thresholding the pixels based solely on cluster size, it is simpler to preserve events that are of interest while discarding the sources of noise coming from particles of a different nature.

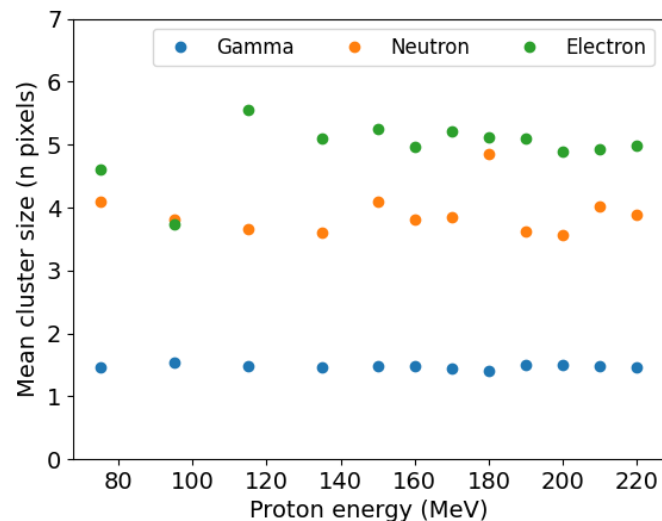


**Figure 6.** Cluster size comparison by particle for each beam energy under study. The figure discriminates between electrons, neutrons and gamma particles.

Ultimately, to validate the hypothesis of achieving the identification of gamma particles only according to the event cluster size, the clusters with a size of up to two pixels were selected for direct comparison with the simulated data coming from particles that are already known to be gammas. This comparison is shown in Figure 7 where the energy deposition spectra are juxtaposed. Although both curves exhibit similar shape and count ranges, the experimental data are slightly skewed towards higher energies and show an increase in counts for energy losses between 100 and 200 keV, which indicates that the discrimination by cluster size, although useful, still shows the effects of the experimental background noise when comparing the experiment to the model.



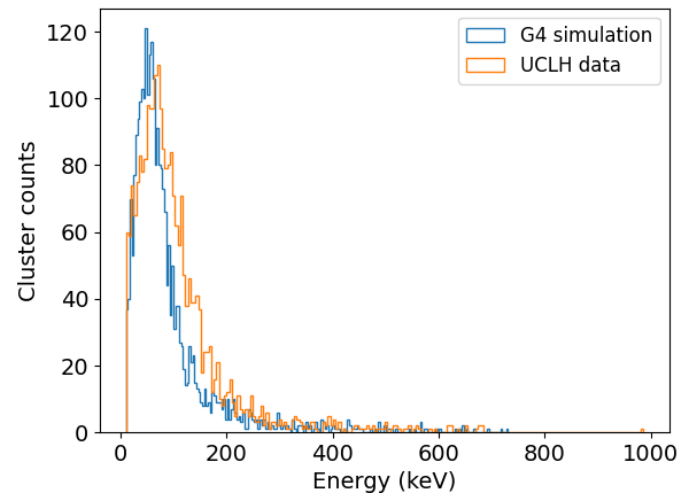


**Figure 7.** Energy loss inside the detector for experimental and simulated data using a proton beam of 150 MeV.

#### 4. Discussion

This study successfully presents and explains the outcomes of the first experiment that was carried out with a HEXITEC detector in a proton therapy environment, where there is evidence of the complexity of the radiation fields produced by the interaction between protons and matter. By comparing the experimental measurements with Monte Carlo simulations, the Geant4 model is an accurate representation of the experiment, meaning that it serves as a useful tool for the future of this research, particularly for the optimisation of detector parameters, without depending on the accessibility of the proton beam at the hospital. However, the comparisons suggest that a further characterisation of the background noise should be performed and included in the model to increase the accuracy. By using the equivalence process described in Section 2.3, a valid standardisation was achieved between HEXITEC frames and Geant4 events. In addition, a way to perform particle discrimination was tested based on solely the cluster size, which can be complemented by further filtering to increase noise reduction, such as more complex algorithms based on machine learning and involving other variables, such as the total energy deposited.

Although constrained by its dimensional limitations, the HEXITEC detector shows promising results in the detection of gamma particles. The low flux reported in the detector area is a result of the dimensions of the detector under study. Fortunately, these values may be enhanced, as recent HEXITEC developments include bigger detector areas and higher frame rates [27,35]. The amount of gammas with the potential to be detected outside of the patient's body have been reported to be low, especially for gammas that are classified as prompt. Thus, the reported statistical data are consistent with previously estimated absolute gamma yields [36]. In addition, the statistical results regarding the percentage contribution of gamma particles show that gamma production depends on the proton beam energy: at lower energies, the contribution of other particles is minimised. This means that when the target volume is located at shallower depths, the background noise coming from other secondary particles is lower, suggesting that prompt gamma imaging could potentially be more accurate in these particular cases, although the difference between energies is not highly significant.

Regarding the classification of cluster events into either a gamma or another particle, the current HEXITEC model has a pixel pitch that enables highly energetic gammas to produce mainly one-pixel clusters, which is indeed helpful for a cluster size analysis that, although simple, is a step towards further reducing the noise coming from undesirable particles to perform prompt gamma imaging in the future. A way to improve cluster classification for future studies involves the implementation of machine learning techniques

that can include not only the size but also the energy deposition per cluster. As the CZT HEXITEC is characterised by its spectral resolution, energy information can be accurately obtained from the sensor and this feature can be further exploited. Nonetheless, this characteristic is highly dependent on the sensor thickness. This means that the system will have to be optimised if a Compton camera is to be built based on HEXITEC detectors. Thus, parameters such as the number of layers, the layer thickness and the possibility of stacking several HEXITEC sensors to increase the sensitive area are the basis of future optimisation studies.

**Author Contributions:** Conceptualisation, R.M.M., M.D.W., B.D.C. and M.L.P.-L.; Experimental data acquisition, J.C.K. and M.D.W.; simulated data production, M.L.P.-L.; data curation, M.L.P.-L.; writing, M.L.P.-L.; review and editing, R.M.M. and M.D.W.; supervision, R.M.M. All authors have read and agreed to the published version of the manuscript.

**Funding:** This research received no external funding.

**Institutional Review Board Statement:** Not applicable.

**Informed Consent Statement:** Not applicable.

**Data Availability Statement:** Not applicable.

**Acknowledgments:** We would like to acknowledge Andy Poynter from the University College London Hospitals NHS Foundation trust, who provided access to the proton beam and supplied details of the proton flux calibration for this experiment.

**Conflicts of Interest:** The authors declare no conflicts of interest.

## References

1. Wilson, R.R. Radiological use of fast protons. *Radiology* **1946**, *47*, 487–491. [[CrossRef](#)]
2. Newhauser, W.D.; Zhang, R. The physics of proton therapy. *Phys. Med. Biol.* **2015**, *60*, R155. [[CrossRef](#)]
3. Kim, P.J.; Shih, H.A. The place of ion beams in clinical applications. In *Ion Beam Therapy*; Springer: Berlin/Heidelberg, Germany, 2012; pp. 17–29.
4. Paganetti, H. Range uncertainties in proton therapy and the role of Monte Carlo simulations. *Phys. Med. Biol.* **2012**, *57*, R99. [[CrossRef](#)]
5. Knopf, A.C.; Lomax, A. In vivo proton range verification: A review. *Phys. Med. Biol.* **2013**, *58*, R131. [[CrossRef](#)]
6. Meißner, H.; Fuchs, H.; Hirtl, A.; Reschl, C.; Stock, M. Towards offline PET monitoring of proton therapy at MedAustron. *Z. Für Med. Phys.* **2019**, *29*, 59–65. [[CrossRef](#)]
7. Knopf, A.; Parodi, K.; Bortfeld, T.; Shih, H.A.; Paganetti, H. Systematic analysis of biological and physical limitations of proton beam range verification with offline PET/CT scans. *Phys. Med. Biol.* **2009**, *54*, 4477. [[CrossRef](#)]
8. Nischwitz, S.P.; Bauer, J.; Welzel, T.; Rief, H.; Jäkel, O.; Haberer, T.; Frey, K.; Debus, J.; Parodi, K.; Combs, S.E.; et al. Clinical implementation and range evaluation of in vivo PET dosimetry for particle irradiation in patients with primary glioma. *Radiother. Oncol.* **2015**, *115*, 179–185. [[CrossRef](#)]
9. Yoshida, E.; Tashima, H.; Shinaji, T.; Shimizu, K.; Wakizaka, H.; Mohammadi, A.; Nishikido, F.; Yamaya, T. Development of a Whole-Body Dual Ring OpenPET for in-Beam PET. *IEEE Trans. Radiat. Plasma Med. Sci.* **2017**, *1*, 293–300. [[CrossRef](#)]
10. Pennazio, F.; Battistoni, G.; Bisogni, M.G.; Camarlinghi, N.; Ferrari, A.; Ferrero, V.; Fiorina, E.; Morrocchi, M.; Sala, P.; Sportelli, G.; et al. Carbon ions beam therapy monitoring with the INSIDE in-beam PET. *Phys. Med. Biol.* **2018**, *63*, 145018. [[CrossRef](#)]
11. Parodi, K. Latest developments in in-vivo imaging for proton therapy. *Br. J. Radiol.* **2020**, *93*, 20190787. [[CrossRef](#)]
12. Lang, K. Towards high sensitivity and high-resolution PET scanners: imaging-guided proton therapy and total body imaging. *Bio-Algorithms Med-Syst.* **2022**, *18*, 96–106. [[CrossRef](#)]
13. Ozoemelum, I.; Van der Graaf, E.; Van Goethem, M.J.; Kapusta, M.; Zhang, N.; Brandenburg, S.; Dendooven, P. Feasibility of quasi-prompt PET-based range verification in proton therapy. *Phys. Med. Biol.* **2020**, *65*, 245013. [[CrossRef](#)]
14. Min, C.H.; Kim, C.H.; Youn, M.Y.; Kim, J.W. Prompt gamma measurements for locating the dose falloff region in the proton therapy. *Appl. Phys. Lett.* **2006**, *89*, 183517. [[CrossRef](#)]
15. Singh, R. *Nuclear Reactions*; New Age International: Delhi, India, 1996.
16. Krimmer, J.; Dauvergne, D.; Letang, J.; Testa, E. Prompt-gamma monitoring in hadrontherapy: A review. *Nucl. Instrum. Methods Phys. Res. Sect. A Accel. Spectrometers Detect. Assoc. Equip.* **2018**, *878*, 58–73.
17. Xie, Y.; Bentefour, E.H.; Janssens, G.; Smeets, J.; Vander Stappen, F.; Hotoiu, L.; Yin, L.; Dolney, D.; Avery, S.; O’Grady, F.; et al. Prompt Gamma Imaging for In Vivo Range Verification of Pencil Beam Scanning Proton Therapy. *Int. J. Radiat. Oncol.* **2017**, *99*, 210–218. [[CrossRef](#)]

18. Pausch, G.; Berthold, J.; Enghardt, W.; Römer, K.; Straessner, A.; Wagner, A.; Werner, T.; Kögler, T. Detection systems for range monitoring in proton therapy: Needs and challenges. *Nucl. Instrum. Methods Phys. Res. Sect. A Accel. Spectrometers Detect. Assoc. Equip.* **2020**, *954*, 161227. [[CrossRef](#)]
19. Terzioglu, F.; Kuchment, P.; Kunyansky, L. Compton camera imaging and the cone transform: A brief overview. *Inverse Probl.* **2018**, *34*, 054002. [[CrossRef](#)]
20. Gutierrez, A.; Baker, C.; Boston, H.; Chung, S.; Judson, D.; Kacperek, A.; Le Crom, B.; Moss, R.; Royle, G.; Speller, R.; et al. Progress towards a semiconductor Compton camera for prompt gamma imaging during proton beam therapy for range and dose verification. *J. Instrum.* **2018**, *13*, C01036. [[CrossRef](#)]
21. Hueso-González, F.; Pausch, G.; Petzoldt, J.; Römer, K.; Enghardt, W. Prompt gamma rays detected with a BGO block Compton camera reveal range deviations of therapeutic proton beams. *IEEE Trans. Radiat. Plasma Med. Sci.* **2016**, *1*, 76–86. [[CrossRef](#)]
22. McCleskey, M.; Kaye, W.; Mackin, D.; Beddar, S.; He, Z.; Polf, J. Evaluation of a multistage CdZnTe Compton camera for prompt  $\gamma$  imaging for proton therapy. *Nucl. Instrum. Methods Phys. Res. Sect. A Accel. Spectrometers Detect. Assoc. Equip.* **2015**, *785*, 163–169. [[CrossRef](#)]
23. Solevi, P.; Munoz, E.; Solaz, C.; Trovato, M.; Dendooven, P.; Gillam, J.E.; Lacasta, C.; Oliver, J.F.; Rafecas, M.; Torres-Espallardo, I.; et al. Performance of MACACO Compton telescope for ion-beam therapy monitoring: First test with proton beams. *Phys. Med. Biol.* **2016**, *61*, 5149. [[CrossRef](#)]
24. Panthi, R.; Maggi, P.; Peterson, S.; Mackin, D.; Polf, J.; Beddar, S. Secondary particle interactions in a Compton camera designed for in vivo range verification of proton therapy. *IEEE Trans. Radiat. Plasma Med. Sci.* **2021**, *5*, 383–391. [[CrossRef](#)] [[PubMed](#)]
25. Veale, M.; Seller, P.; Wilson, M.; Liotti, E. HEXITEC: A high-energy X-ray spectroscopic imaging detector for synchrotron applications. *Synchrotron Radiat. News* **2018**, *31*, 28–32. [[CrossRef](#)]
26. Wilson, M.; Dummott, L.; Duarte, D.D.; Green, F.; Pani, S.; Schneider, A.; Scuffham, J.; Seller, P.; Veale, M. A 10 cm  $\times$  10 cm CdTe Spectroscopic Imaging Detector based on the HEXITEC ASIC. *J. Instrum.* **2015**, *10*, P10011. [[CrossRef](#)]
27. Jowitt, L.; Wilson, M.; Seller, P.; Angelsen, C.; Wheeler, R.; Cline, B.; Schöne, D.; Lauba, F.; Goede, M.; Ball, R.; et al. HEXITEC 2  $\times$  2 tiled hard X-ray spectroscopic imaging detector system. *J. Instrum.* **2022**, *17*, P01012. [[CrossRef](#)]
28. Scuffham, J.W.; Wilson, M.D.; Pani, S.; Duarte, D.D.; Veale, M.C.; Bell, S.; Seller, P.; Sellin, P.J.; Cernik, R.J. Evaluation of a new small-pixel CdTe spectroscopic detector in dual-tracer SPECT brain imaging. In Proceedings of the 2012 IEEE Nuclear Science Symposium and Medical Imaging Conference Record (NSS/MIC), Anaheim, CA, USA, 29 October–3 November 2012; pp. 3115–3118. [[CrossRef](#)]
29. Zhang, J.; Zannoni, E.M.; Du, Y.; Frey, E.; Meng, L.J. Alpha-SPECT: Hyperspectral single photon imaging of targeted  $\alpha$ -emission therapy. *J. Nucl. Med.* **2019**, *60*, 311.
30. Granja, C.; Jakubek, J.; Polansky, S.; Zach, V.; Krist, P.; Chvatil, D.; Stursa, J.; Sommer, M.; Ploc, O.; Kodaira, S.; et al. Resolving power of pixel detector Timepix for wide-range electron, proton and ion detection. *Nucl. Instrum. Methods Phys. Res. Sect. A Accel. Spectrometers Detect. Assoc. Equip.* **2018**, *908*, 60–71. [[CrossRef](#)]
31. Agostinelli, S.; Allison, J.; Amako, K.A.; Apostolakis, J.; Araujo, H.; Arce, P.; Asai, M.; Axen, D.; Banerjee, S.; Barrand, G.; et al. GEANT4—A simulation toolkit. *Nucl. Instrum. Methods Phys. Res. Sect. A Accel. Spectrometers Detect. Assoc. Equip.* **2003**, *506*, 250–303. [[CrossRef](#)]
32. Chen, Z.; Yang, P.; Lei, Q.; Wen, Y.; He, D.; Wu, Z.; Gou, C. Comparison of BNCT dosimetry calculations using different GEANT4 physics lists. *Radiat. Prot. Dosim.* **2019**, *187*, 88–97. [[CrossRef](#)]
33. Wrońska, A.; Kasper, J.; Ahmed, A.A.; Andres, A.; Bednarczyk, P.; Gazdowicz, G.; Herweg, K.; Hetzel, R.; Konefał, A.; Kulesa, P.; et al. Prompt-gamma emission in GEANT4 revisited and confronted with experiment. *Phys. Med.* **2021**, *88*, 250–261. [[CrossRef](#)]
34. Kramer, O. Scikit-learn. In *Machine Learning for Evolution Strategies*; Springer: Berlin/Heidelberg, Germany, 2016; pp. 45–53.
35. Jones, L.; Bell, S.; Cline, B.; Gardiner, T.; Hart, M.; Prydderch, M.; Seller, P.; Veale, M.; Wilson, M. Spectroscopic X-ray imaging at MHz frame rates—The HEXITECMHz ASIC. *J. Instrum.* **2022**, *17*, C10012. [[CrossRef](#)]
36. Pinto, M.; Bajard, M.; Brons, S.; Chevallier, M.; Dauvergne, D.; Dedes, G.; De Rydt, M.; Freud, N.; Krimmer, J.; La Tessa, C.; et al. Absolute prompt-gamma yield measurements for ion beam therapy monitoring. *Phys. Med. Biol.* **2014**, *60*, 565. [[CrossRef](#)] [[PubMed](#)]

**Disclaimer/Publisher’s Note:** The statements, opinions and data contained in all publications are solely those of the individual author(s) and contributor(s) and not of MDPI and/or the editor(s). MDPI and/or the editor(s) disclaim responsibility for any injury to people or property resulting from any ideas, methods, instructions or products referred to in the content.